ACS OMEGA

Open Access

http://pubs.acs.org/journal/acsodf

Article

Mechanical Properties of a Honeycomb Structure Dispersed with 3D-Printed Fe_3O_4 Nanomaterials

Xinhua Song, Shize Hong, Jing Wang, Xinyu Zhu, Shudong Guo, Yanshu Fu,* Yixuan Yang, Ming Yang, Wuyi He, Yu Tang, and Binlun Gao

Cite This: *ACS Omega* 2024, 9, 14287−14296

Read Online

ACCESS | Metrics & More | Article Recommendations

ABSTRACT: The honeycomb structure demonstrates exceptional stability, efficient mechanical performance, outstanding load-bearing capacity, and energy-saving and lightweight properties, rendering it extensively employed in various fields such as industrial manufacturing, radiation protection building, aerospace engineering, and wave-absorbing stealth materials. Bionic design can enhance the performance of structures, making bionic honeycomb design valuable in engineering. This study employs a bionic optimization design based on the original honeycomb size to investigate the impact of a new composite honeycomb core structure on mechanical properties. Orthogonal experiments are conducted to explore the effect of honeycomb size on mechanical properties and determine the optimal size. Combining numerical simulation and 3D printing experiments, we examine the mechanical properties of both nano-Fe_3O_4 particle-distributed honeycomb structure and common structures, analyzing mechanisms behind their tensile and compressive properties.

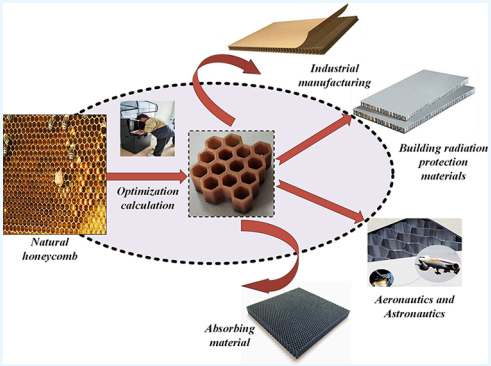

1. INTRODUCTION

The aerospace industry is witnessing a growing need for multifunctional solutions due to rapid progress in equipment manufacturing technology. In addition to requirements for lightweight, high durability, and reliability, new aviation materials are also evolving toward multipurpose applications, high performance capabilities, novel technologies, cost-effectiveness, and innovative concepts.[1,2] Composite materials possess numerous advantages over traditional metal materials in terms of performance and functionality, hence they are increasingly being employed across various sectors within the aviation industry.[3] As material engineering progresses alongside advancements in manufacturing technology, a plethora of lightweight structures have been developed with honeycomb structures emerging as one such example.[4] After years of development and optimization design efforts, honeycomb structures have found widespread utilization within the aerospace domain. However, to meet diverse specifications and criteria, these optimized honeycomb structures have become significantly more complex in their own architecture, thereby posing challenges during processing and manufacturing stages. Traditional milling and grinding methods struggle to fabricate suitable structures while additive manufacturing technology (3D printing) has gained prominence due to its robust production capabilities.[5−9]

The honeycomb structure is extensively employed owing to its lightweight, exceptional specific stiffness and strength, remarkable impact resistance, high shear modulus, excellent heat and noise insulation properties, robust designability, and other notable characteristics.[10,11] Moreover, the low unit volume loss factor of porous materials in honeycomb structures can reduce stress concentration and exhibit excellent electromagnetic performance for radomes and radar domes.[12] By optimizing the design or incorporating composite materials into honeycomb structures, they can achieve superior thermal insulation, impact resistance, vibration reduction, sound absorption, and stealth capabilities. In aerospace applications specifically for aircraft, stealth designs using honeycomb sandwich structures not only ensure load-carrying capacity but also provide antenna equipment placement within the sandwich structure to improve overall aircraft performance.

Driven by the increasingly stringent demands of engineering applications, a considerable body of research has been conducted over the past two decades to investigate the fundamental mechanical response of honeycomb materials under tensile, compressive, shear, and fatigue loads. Song et al.[13] performed experimental tests on the mechanical proper-

Received: December 18, 2023
Revised: February 27, 2024
Accepted: March 4, 2024
Published: March 14, 2024

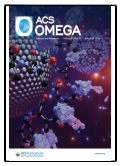

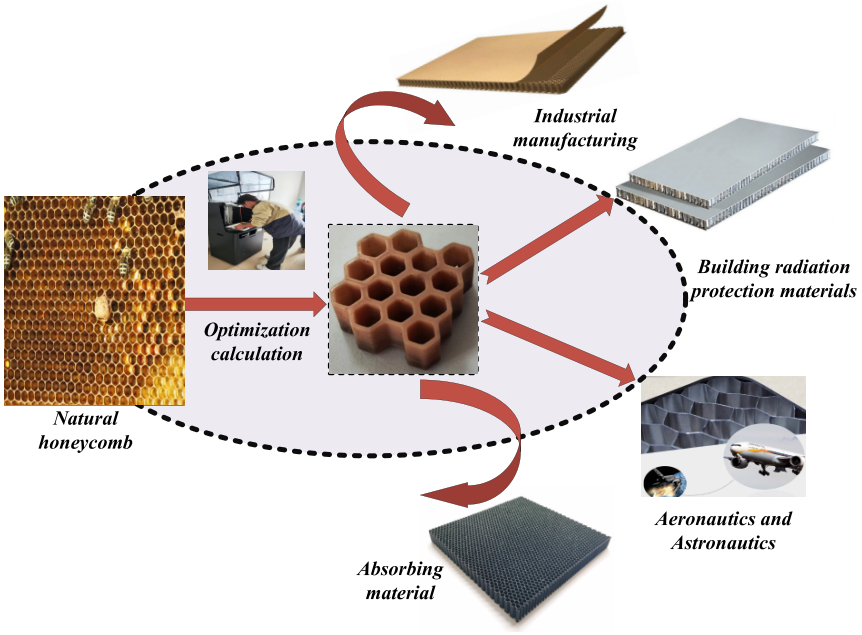

Figure 1. A schematic diagram illustrating the optimization calculation, preparation, and application of the natural honeycomb mechanical properties.

ties of composite interlocking diamond honeycomb (CIDH) and its sandwich structure (CIDHSS), analyzing the stiffness, strength, and failure characteristics of CIDH and CIDHSS. Hegde and Hojjati[14] examined microcracks in composite honeycomb sandwich structures and their impact on mechanical properties while proposing a method to assess the extent of mechanical strength degradation under thermal fatigue.

Du et al.[15] investigated parameter optimization and mechanical properties of Ti_2AlNb-based alloy honeycomb structures prepared through a superplastic forming/diffusion bonding (SPF/DB) process, conducting uniaxial tensile tests at various temperatures and strain rates. Xia et al.[16] explored 3D printing technology for designing and manufacturing a novel double-layer helical honeycomb (DLHH), investigating its in-plane mechanical properties as well as energy absorption capacity using both experimental and simulation approaches. Zhong et al.[17] designed, fabricated, and studied an innovative concrete composite material with expanded layered honeycomb to examine the load-bearing performance of expanded metamaterials under quasi-static compression conditions. The layered honeycomb sandwich structure was analyzed through quasi-static compression testing, while evaluating its energy absorption capability. Dong et al.[18] fabricated two typical thin-walled and thick-walled concave hexagonal honeycombs and conducted compression tests to characterize the deformation patterns, distributions of negative Poisson's ratio, and extrusion stresses. Xu et al.[19] combined recessed aluminum honeycomb with aluminum foam and performed experimental and numerical investigations on the mechanical properties and deformation patterns of recessed aluminum honeycomb filled with aluminum foam. Additionally, the effects of geometric parameters of such honeycombs are also studied. Zhang et al.[20] developed dynamic compression tests to investigate the dynamic compression mechanical properties of aluminum honeycomb structures at different strain rates, particularly at high strain rates. Lvov et al.[21] examined the Poisson's ratio of recessed honeycomb structures by integrating theoretical calculations, computer simulations, and experimental evaluations to determine optimal unit parameters for 3D-printed samples made from thermoplastic polyurethane (TPU). Luo et al.[22] investigated the enhancement in mechanical properties of recessed honeycombs by filling them with a buffer material called slow recovery foam; numerical simulation and experiments were employed to study the mechanical properties and deformation behavior of slow recovery foam-filled recessed honeycombs. Hou et al.[23] conducted a mechanical analysis on hyperbolic sandwich structures using an equivalent model approach; detailed models based on sandwich theory as well as bending sandwich theory were established for a hyperbolic sandwich engine cover composed of two carbon fiber-reinforced plastic (CFRP) skins and a Nomex honeycomb core, which is designed and optimized based on traditional aluminum alloy engine covers.

The methods employed for investigating the mechanical properties of honeycomb primarily encompass experimental testing, numerical simulation, theoretical analysis, and empirical and semiempirical fitting, among others. Furthermore, topological structure optimization design techniques are utilized to enhance the mechanical properties of honeycomb materials under diverse objectives and constraints.[24,25] Thanks to nature's inspiration and human ingenuity, there has been a significant advancement in the mechanical properties of honeycomb materials. Bionic structural design is regarded as a promising strategy for augmenting the mechanical properties and energy absorption capabilities of lightweight honeycomb materials. In this study, we explore the impact of a novel composite honeycomb core structure on its mechanical properties through bionic optimization design based on the original honeycomb size. This research provides a theoretical reference for employing honeycomb structures in various fields such as industrial manufacturing, radiation-proof construction, aerospace engineering, and wave-absorbing stealth materials[17,26−31] (as depicted in Figure 1), thereby serving as a foundation for optimizing the mechanical properties of 3D-printed Fe_3O_4 nanocomposite honeycombs. Additionally, it

https://doi.org/10.1021/acsomega.3c10138
ACS Omega 2024, 9, 14287−14296

offers theoretical guidance for future applications in military and civilian scenarios.

2. RESULTS AND DISCUSSION

2.1. Influence of Honeycomb Size Effect on Mechanics. The influence of the sample size on the experimental results is a crucial aspect in mechanical testing of honeycomb materials. The mechanical properties of porous materials are influenced by various factors including the matrix material attributes, geometric characteristics of the pores, and other parameters. Due to the unique structure of porous materials, their mechanical behavior often exhibits a size effect within a specific range of sample sizes. Song et al.[32] investigated the impact of structural size on bending characteristics of PKCSS and discussed variations in bending strength and stiffness, ultimately determining optimal size design ratios and recommendations. Jin et al.[33] conducted uniaxial compression tests on three honeycomb samples with different relative densities to study how in-plane sample dimensions affect the mechanical properties of hexagon honeycombs. Pham and Hütter,[34] using direct numerical simulation (DNS) for mesostructure analysis, examined how porosity, pore shape, and material distribution along support and load directions affect both size effect and effective modulus in regular honeycomb structures. While previous studies have focused on in-plane dimensions only, this comprehensive investigation considers both in-plane and out-of-plane dimensions due to their combined influence on the mechanical properties.

First, based on the data presented in Table 1, variance analysis is conducted to determine the average value and intergroup variation for each group. Subsequently, the range is introduced to quantify the extreme values between M_{max} and M_{min} of each factor, denoted as N. The magnitude of N indicates the degree of influence that each factor has on the physics ability. The results of the finite element orthogonal experiment are summarized in Table 2. Building upon these findings, an analysis of size effect in honeycomb sandwich structures is performed, leading to selection of optimal structural combination parameters tailored to specific requirements for each index. Under identical displacement loads, it is observed that higher peak internal stress values indicate superior tensile resistance within practical applications by effectively mitigating stress concentration phenomena. Additionally, minimal axial deformation signifies enhanced stiffness characteristics exhibited by honeycomb sandwich structures, which contribute to improved load-bearing performance and stability while minimizing susceptibility to fracture.

Table 1. Orthogonal Experimental Analysis

experiment number	factor-level combination			internal stress peak of structure (MPa)	axial deformation (mm)	shrinkage of section (%)
1	A1	B1	C1	5.081	2.992	24.281
2	A1	B2	C2	4.847	2.123	22.863
3	A1	B3	C3	4.794	2.098	25.110
4	A2	B1	C2	5.039	2.999	25.552
5	A2	B2	C3	4.829	2.404	23.275
6	A2	B3	C1	4.770	2.347	25.123
7	A3	B1	C3	4.836	3.009	23.873
8	A3	B2	C1	4.824	2.334	23.708
9	A3	B3	C2	4.851	2.619	23.277

Second, considering the influence of the axial deformation level, for the average value M, the maximum M3 value of factor A is 4.908 MPa, indicating that at level A3, the axial deformation is most pronounced and exhibits superior extension in regular hexagon honeycomb structure. Similarly, factor B demonstrates a larger M1 value, whereas for factor C, the largest M2 value is observed at the same level. Therefore, taking into account the axial deformation index, the optimal size combination for honeycomb sandwich structures would be A3, B1, and C2. Observing range N reveals that NB has the greatest impact, while NC has minimal influence; NA falls between these two extremes. Thus, factors affecting axial deformation are ranked as follows: bee lattice side length—bee wall thickness—honeycomb height.

In general, the size effect of a honeycomb structure can be categorized into in-plane and out-of-plane size effects. The in-plane size effect refers to the influence of parameters such as honeycomb wall thickness and inner side length on the overall mechanical behavior of a honeycomb sandwich structure.[32] On the other hand, the out-of-plane size effect considers factors like height, direction, and dimensional ratios that affect the mechanical behavior of a honeycomb sandwich structure. For regular hexagonal honeycombs, both wall thickness (t) and lattice side length (L) have significant impacts on various equivalent elastic parameters.[35] To investigate the mechanical behavior and in-plane size effect of regular hexagon honeycombs, we employed a control variable method with a fixed height (H = 34 mm). Our study revealed that increasing the ratio of wall thickness to side length initially increased and then decreased peak internal stress values within the structure. Axial deformation exhibited an increasing trend, while sectional shrinkage rate showed a continuous decrease. These findings indicate an evident in-plane size effect for honeycomb sandwich structures. Notably, when the ratio of wall thickness to side length was 0.49, maximum stress peaked at 5.081 MPa with axial deformation showing an increasing trend, while sectional shrinkage displayed decreasing tendencies. Therefore, it is concluded that this particular structural configuration exhibits superior mechanical performance when maintaining a ratio of wall thickness to side length at 0.49, consistent with optimal structural sizing parameters obtained from previous analyses.

Table 2. Average and Range Statistics

	peak stress (MPa)			axial deformation (mm)			shrinkage of section (%)		
analysis index	A	B	C	A	B	C	A	B	C
M1	4.908	4.985	4.892	2.404	3.000	2.558	24.085	24.569	24.371
M2	4.879	4.833	4.912	2.583	2.287	2.580	24.560	23.282	23.890
M3	4.837	4.805	4.820	2.654	2.354	2.503	23.619	24.503	24.086
N3	0.071	0.180	0.092	0.250	0.713	0.077	0.941	1.287	0.481

https://doi.org/10.1021/acsomega.3c10138
ACS Omega 2024, 9, 14287−14296

Subsequently, while maintaining a honeycomb wall thickness of t = 0.49 mm, the aspect ratio (L/H) of the honeycomb hole wall is varied within the range of 0.0263 to 0.0882. The investigation into this side length/height ratio clearly revealed a significant out-of-plane size effect on the mechanical performance of the honeycomb sandwich structure. Notably, at an aspect ratio of 0.0294, the maximum peak stress reached 5.042, indicating optimal mechanical performance and justifying its selection for further research.

2.2. Tensile and Compression Numerical Simulation Analysis of the Honeycomb Structure. Based on the numerical simulation results of tensile and compressive tests shown in Figure 2a–d, it can be observed that the fracture of

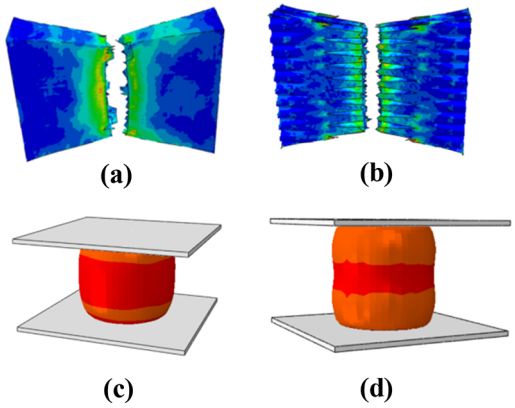

Figure 2. The Mises stress nephogram, illustrating (a) the standard tensile model, (b) the honeycomb core tensile model, (c) the standard compression model, and (d) the honeycomb core compression model.

the tensile specimen occurs at its weak center. The standard specimen has a tensile strength of 17.6517 MPa, while the honeycomb core tensile specimen has a strength of 10.7393 MPa, which is approximately 60.84% lower than that of the standard specimen. Similarly, the compressive strength of the honeycomb core compression specimen is about 14.14% compared with that of the standard specimen (137.312 MPa). Comparison between numerical simulation curves and experimental data (Figure 3 and Table 3) reveals good agreement between them with minor discrepancies due to uneven internal material distribution within some test specimens, leading to absence or reduction in yield enhancement stage.

2.3. Experimental Analysis of Tensile and Compressive Properties of the Nano-Fe_3O_4 Dispersed Honeycomb Structure. In this study, two sets of samples are prepared: one set consisted of pure resin material tensile and compression specimens, while the other set comprised printed specimens with a 1% content of nano-Fe_3O_4. Tensile and compression experiments were conducted using a universal testing machine, and the stress–strain curves for both groups are presented in Figure 4. Subsequently, by replacing the working section of the standard tensile specimen with a honeycomb core, we found a significant decrease in both tensile and compression performance. The cross-sectional sizes of the fracture points for both groups are calculated during the experiment. Under tensile testing conditions, $S_{standard}$ = 290 mm^2, $S_{honeycomb}$ = 167.08 mm^2, thus obtaining a comparison chart depicting the stress–strain curves for both cases. The original specimen exhibited a tensile strength of 17.673 MPa, whereas the honeycomb core specimen displayed a reduced value of 10.794 MPa (61.08% compared to the standard specimen). Under compression testing conditions, $S_{honeycomb}$ = 127.87 mm^2, $S_{standard}$ = 213.82 mm^2, resulting in an original specimen's compressive strength value of 144.0868 MPa and that for the honeycomb core specimen of 19.8104 MPa (13.75% compared to the standard specimen).

2.4. Analysis of Tensile and Compressive Properties of Honeycomb Structures Dispersed by Nano-Fe_3O_4. In summary, the incorporation of nano-Fe_3O_4 particles into photosensitive resin demonstrates a significant enhancement in the material compressive strength. However, under axial tensile forces, the stress concentration becomes exacerbated, leading to uneven distribution of Fe_3O_4 particles within the material and resulting in increased susceptibility to fracture and failure. Consequently, the desired improvement in tensile performance is not achieved. The specific mechanism is illustrated in Figure 5.

First, the organic combination of nano-Fe_3O_4 particles and a photosensitive resin base exhibits poor compatibility. In the absence of a strong magnetic field, Fe_3O_4 nanoparticles tend to strongly attract each other, making it challenging to achieve uniform dispersion of the polymer-based magnetic material within the resin matrix and leading to agglomeration.[36,37] Additionally, the fracture extension performance of the resin matrix typically surpasses that of nano-Fe_3O_4 particles, resulting in initial fracture occurring within the agglomerated Fe_3O_4 particle structure.[38,39] Subsequent to aggregate fracture, stress originally borne by the aggregate is transferred simultaneously to both the composite material consisting of a resin matrix and fractured regions surrounding Fe_3O_4 particle matrices. Consequently, numerous stress concentration points emerge. The deformation ability and toughness of the utilized photosensitive resin base are insufficient for resisting or dispersing stress concentrations caused by its own fractures. This ultimately leads to rapid crack propagation until tensile failure occurs in a brittle fashion, thereby reducing both tensile strength and overall mechanical properties upon incorporation of nano-Fe_3O_4 particles.

Furthermore, the addition of nanoparticles to the resin matrix in composite materials leads to a reduction in the force area of the resin per unit size. In cases where there is poor interface bonding between the nanoparticles and the resin matrix, external forces can easily cause interface debonding and separation. This phenomenon contributes to the lower tensile strength observed in filled composite specimens compared with pure resin specimens.

Finally, in the compressed state, the photosensitive resin material can be considered as a coating effect on nano-Fe_3O_4 particles. The inner and outer surfaces of the material exhibit high density, effectively dispersing stress caused by interface slip resulting from an uneven distribution of the material. Consequently, when external force is applied to the Fe_3O_4 nanocomposite, it provides protection to the matrix resin against easy crushing and enhances its compressive strength. Moreover, due to their superior mechanical strength at the nanoscale compared to that of photosensitive resin materials, iron oxide particles further contribute to the improved compressive strength of Fe_3O_4 nanocomposites. Compared with pure resin counterparts, this composite exhibits an impressive 280.08% increase in compressive strength.

https://doi.org/10.1021/acsomega.3c10138
ACS Omega 2024, 9, 14287–14296

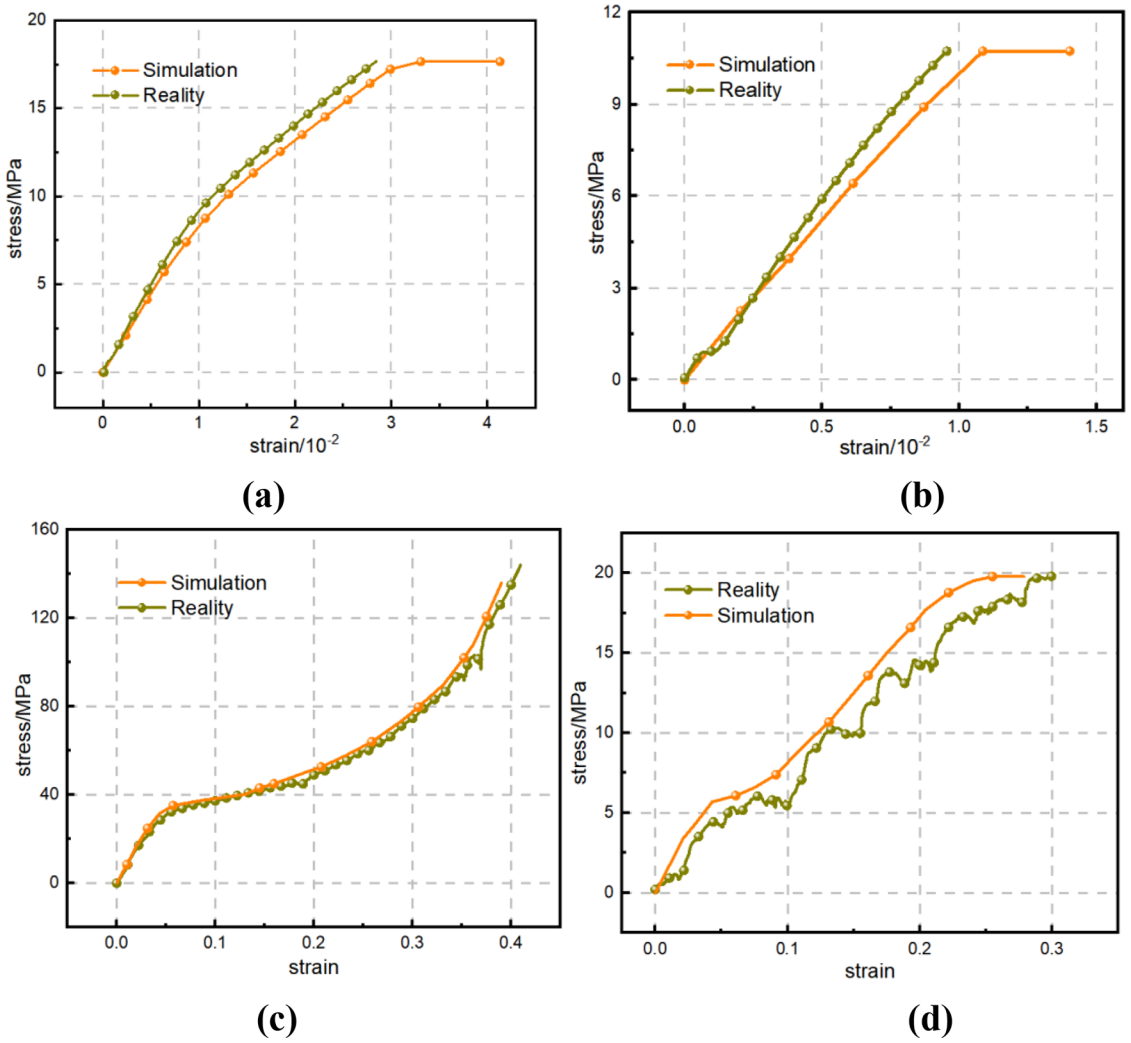

Figure 3. A stress−strain comparison between tensile and compression tests, showcasing different specimen types for each test. Specifically, (a) illustrates the standard tensile specimen while (b) depicts the honeycomb tensile specimen. On the other hand, (c) represents the standard compression specimen whereas (d) showcases the honeycomb compression specimen.

Table 3. Comparison of Tensile and Compression Simulation and Real Experimental Compressive Strength

deformation form	calculation method	specimen type	intensity (MPa)	error (%)
specimen drawing	numerical simulation	standard specimen	17.6517 MPa	39.15%
		honeycomb core specimen	10.7393 MPa	
	experiment	standard specimen	17.673 MPa	39.09%
		honeycomb core specimen	10.794 MPa	
specimen compression	numerical simulation	standard specimen	137.312 MPa	14.14%
		honeycomb core specimen	19.412 MPa	
	experiment	standard specimen	144.087 MPa	13.75%
		honeycomb core specimen	19.810 MPa	

3. CONCLUSIONS AND OUTLOOK

The present study investigates the influence of a novel composite honeycomb core structure on mechanical properties through a bionic optimization design based on the original honeycomb dimensions. First, an analysis is conducted to examine the influence of honeycomb size effect on mechanical properties using orthogonal experiments. Subsequently, numerical simulation and 3D printing experiments are employed to investigate the mechanical properties of nano-Fe_3O_4 particle-infused honeycomb structures, thereby revealing their underlying mechanisms.

The factors influencing the axial deformation of the honeycomb structure are ranked in descending order as follows: the side length of the honeycomb lattice, wall thickness, and height of the honeycomb. Optimal mechanical performance is achieved when the ratio of wall thickness to side length is 0.49 and the ratio of side length to height is 0.0294. The tensile strength of the standard specimen measures 17.6517 MPa, while that of the honeycomb core tensile specimen reaches 10.7393 MPa, accounting for approximately 60.84% of the standard specimen's strength. In terms of compressive strength, the standard specimen

https://doi.org/10.1021/acsomega.3c10138
ACS Omega 2024, 9, 14287−14296

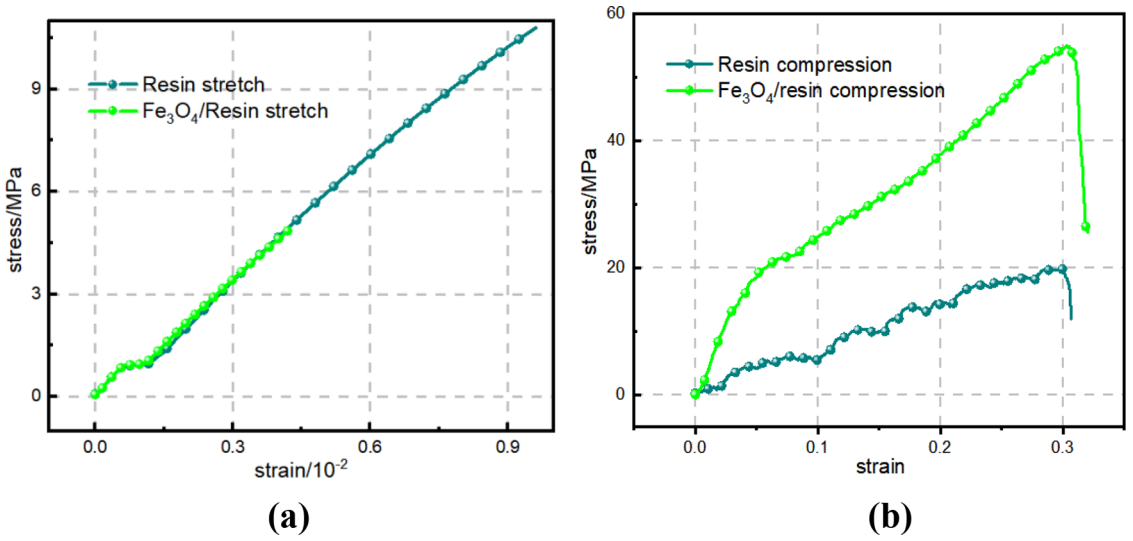

Figure 4. (a) The stress−strain curve obtained from the tensile test, (b) the stress−strain curve derived from the compression test.

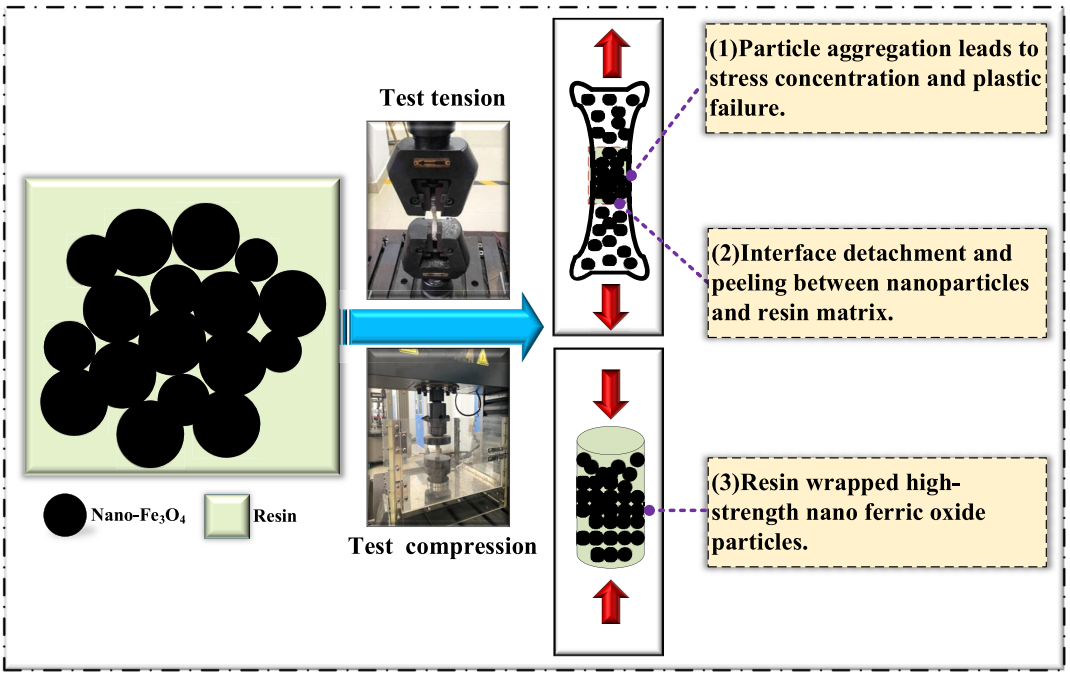

Figure 5. A schematic diagram depicting the tensile mechanical properties of a honeycomb structure dispersed with nano-Fe_3O_4, in accordance with academic and professional standards.

records a value of 137.312 MPa compared to only 19.412 MPa for the honeycomb core compressive specimen, which represents about 14.14% relative to that of the standard specimen.

In this paper, several challenges persist in the investigation of mechanical properties of nano-Fe_3O_4 particle-walk honeycomb structures. For instance, further investigation is required to optimize the coordination design of the honeycomb size for weight reduction, material conservation, and enhanced mechanical properties. Additionally, there is a need for a deeper understanding of the energy absorption mechanism in honeycombs under different loading directions. The manufacturing technology for complex honeycombs remains challenging, and the limited application of advanced design hampers improvements in honeycomb characteristics. Given the current progress in research on 2D chiral honeycomb structures as mechanical metamaterials, exploring micro machining theory from a 3D perspective holds significant importance for designing, manufacturing, and applying metamaterials.

4. EXPERIMENTAL SECTION

4.1. Numerical Simulation. The mechanical properties of the honeycomb structure are numerically simulated using Abaqus in this study. To ensure comparability of results despite model irregularities, a four-node quadrilateral element is employed for free-form grid division, while three-grid mapping is applied to the boundary surface of the model. The material parameters for input PROPERTY are presented in Table 4, and a consistent hexagonal element is utilized for

https://doi.org/10.1021/acsomega.3c10138
ACS Omega 2024, 9, 14287−14296

structural grid division when the compression model is divided into grids.

Table 4. Regular Hexagonal Honeycomb Numerical Model Material Parameters[40]

photosensitive resin	Young's modulus (MPa)	density (kg/m^3)	Poisson's ratio
numerical value	1827 MPa	1116.7 kg/m^3	0.395

The honeycomb model exhibits a wall thickness of 0.49 mm and a beehive side length of 1 mm, as depicted in Figure 6a. A

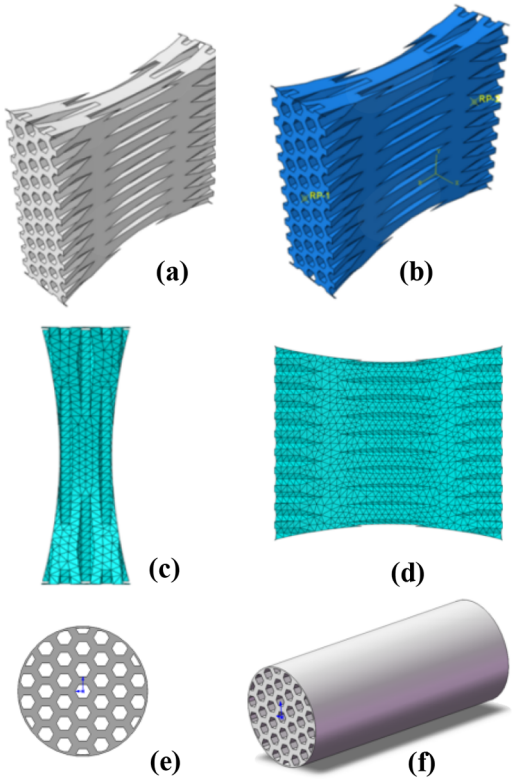

Figure 6. (a) Tensile finite element model of the honeycomb core. (b) Schematic diagram illustrating reference points. (c) Upper view depicting the partition mesh of the model. (d) Side view displaying the partition mesh of the model. (e) Front view showcasing the compressed model. (f) Side view presenting the compressed model.

finite element analysis (FEA) model is developed to simulate the tensile testing of the honeycomb core using standard specimen dimensions. Displacement loading is employed to replicate the tensile performance of the honeycomb structure. The model incorporates reference points RP-1 for load application and RP-2 for constraint application, which are coupled to the contact surface to establish boundary conditions. As shown in Figure 6b, an 8 mm displacement load is applied at the end of RP-1 while all constraints are imposed at the end of RP-2. To account for irregularities in the model, free-form grid division utilizing four-node quadrilateral elements is implemented along with a mapped three-grid on the boundary surface of the structure. Figure 6c,d illustrates the adopted grid division scheme for modeling the honeycomb core specimen, consisting of a total node count of 71,362 and an element grid count of 40,867.

The compression model was established by SOLIDWORKS, as illustrated in Figure 6e,f. The model utilized a hexagonal grid consisting of 16,560 grids and 25,051 nodes. A honeycomb structure with a wall thickness of 0.49 mm and a side length of 1 mm was constructed. Incompressible rigid bodies were assigned to the top and bottom surfaces for compression analysis.

4.2. Orthogonal Experiment. The orthogonal experimental design[41−43] is a systematic approach that investigates multiple factors and levels by selecting representative points based on orthogonality. These selected points exhibit characteristics of "uniform dispersion, organization, and comparability". According to the three factors influencing the mechanical properties of honeycomb sandwich structures, an orthogonal experimental design with three factors and three levels is implemented (Table 5). The L9(3^4) orthogonal table

Table 5. Factor-Level Design Table for the Orthogonal Test

	factor A	factor B	factor C
level	bee wall thickness (mm)	bee cell side length (mm)	cell height (mm)
1	0.29	1	30
2	0.49	2	34
3	0.70	3	38

Table 6. Experimental Grid Selection (n = 3)

experiment number	1	2	3	4	5	6	7	8	9
factor A	1	1	1	2	2	2	3	3	3
factor B	1	2	3	1	2	3	1	2	3
factor C	1	2	3	2	3	1	3	1	2

(Table 6) is utilized for this purpose. Based on the orthogonal table, a corresponding experimental model is established, as depicted in Figure 7. A displacement load of 3 mm is applied to measure the peak internal stress, axial deformation, and sectional shrinkage rate of each structural group. The obtained experimental results are presented in Table 1.

4.3. 3D Printing Preparation. The SLA printing equipment HALOT-MAX is utilized in this study, with the experimental material being the white photosensitive resin produced by CREALITY. The design dimensions of the tensile specimen are presented in Figure 8a,[44] while those of the compression specimen can be found in Figure 8b.[45] It is important to note that the height direction corresponds to the Z-axis, which represents the force applied during compression experiments.

Considering the precision and printing range of the 3D printer, a compression specimen with a diameter (D) of 4 mm and a height (H) of 10 mm is selected. The 3D printing parameters are presented in Table 7, where the support density for the compression specimen is set to 70%. The printed specimen entities are depicted in Figure 8c−f. In Figure 8e,f, it can be observed that nano-Fe_3O_4 particles are added at a concentration of 40 wt %, with an average size of approximately 20 nm. A stirrer is employed to agitate the mixture at a speed of 300 r/min for a duration of 10 min. Following completion of stirring, the mixed slurry is stored in an opaque container to prevent exposure to light during subsequent experiments. Due to the composite material's

https://doi.org/10.1021/acsomega.3c10138
ACS Omega 2024, 9, 14287−14296

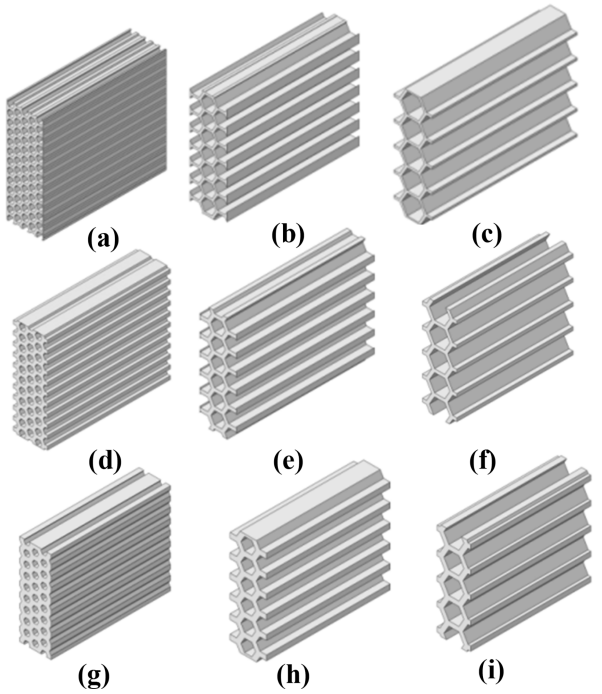

Figure 7. Orthogonal experimental model (a−i represent experiments 1−9, respectively).

limited flowability and susceptibility to light irradiation difficulties, the support printing density is increased to 75%, as detailed in Table 7.

Table 7. Optimal Parameters and Support Parameter Settings for the 3D Printing of Specimens

print parameter		support parameter	
layer thickness	0.050 mm	support type	middle part
initial exposure	50 s	height from platform	6.00 mm
print exposure	3 s	support density	60% (70%)
print rise rate	8 mm	center diameter	0.50 mm
motor speed	2 mm/s	support diameter	1.50 mm
lamp delay	6 s	add base	Y
the number of layers of underlying exposure	2	overhang only	N

Upon completion of the printing process, the printing blank is removed and any partially solidified resin residue on the specimen's surface is rinsed with anhydrous ethanol and subsequently dried for 48 h. The support structure is then detached from the specimen using a file and other appropriate tools, followed by a suitable grinding treatment based on specific experimental requirements. Alternatively, the specimen can undergo secondary irradiation curing in a light-curing printer to enhance the stability of its performance. Surface topography analysis reveals that it exhibits a dense and finely textured appearance without any noticeable cracks or agglomeration, as depicted in Figure 8e,f.

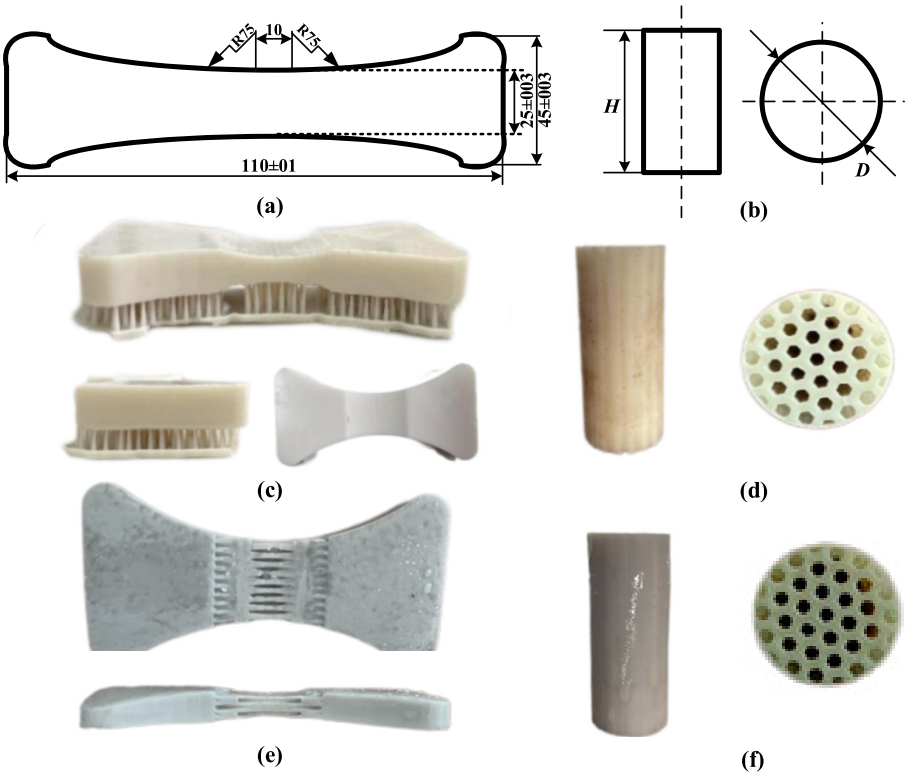

Figure 8. (a) The detailed dimensional parameters of the III-shaped tensile specimen. (b) The detailed dimensional parameters of the compression specimen. (c) A three-dimensional view of the honeycomb core tensile specimen. (d) The honeycomb core compression specimen. (e) The tensile specimen of Fe_3O_4 nanocomposites' honeycomb structure. (f) The compressed specimen of Fe_3O_4 nanocomposites' honeycomb knot.

https://doi.org/10.1021/acsomega.3c10138
ACS Omega 2024, 9, 14287−14296

■ ASSOCIATED CONTENT

Data Availability Statement

Research data are not shared.

■ AUTHOR INFORMATION

Corresponding Author

Yanshu Fu − *School of Advanced Manufacturing, Nanchang University, Nanchang 330031, China*; Email: yshfu@ncu.edu.cn

Authors

Xinhua Song − *School of Infrastructure Engineering, Nanchang University, Nanchang 330031, China*; orcid.org/0000-0002-8232-6869

Shize Hong − *School of Infrastructure Engineering, Nanchang University, Nanchang 330031, China*

Jing Wang − *Taian Special Equipment Inspection and Research Institute, Taian 271000, China*

Xinyu Zhu − *School of Infrastructure Engineering, Nanchang University, Nanchang 330031, China*

Shudong Guo − *Taian Special Equipment Inspection and Research Institute, Taian 271000, China*

Yixuan Yang − *School of Infrastructure Engineering, Nanchang University, Nanchang 330031, China*

Ming Yang − *China Non-metal Materials Mine Engineering Co., Ltd. (Nanjing), Nanjing 210094, China*

Wuyi He − *Jiangxi Rongda New Blasting Technology Development Co., Ltd., Nanchang 330000, China*

Yu Tang − *School of Infrastructure Engineering, Nanchang University, Nanchang 330031, China*

Binlun Gao − *School of Infrastructure Engineering, Nanchang University, Nanchang 330031, China*

Complete contact information is available at: https://pubs.acs.org/10.1021/acsomega.3c10138

Author Contributions

Y.F. conceived and designed the experiments and supervised the complete study. X.S., S.H., J.W., X.Z., S.G., Y.Y., M.Y., W.H., Y.T., and B.G. prepared the samples, performed the experiments, and collected the data. Both the authors analyzed the data, wrote the manuscript, and agreed to the published version of the manuscript.

Notes

The authors declare no competing financial interest.

■ ACKNOWLEDGMENTS

This project was financially supported by the National Natural Science Foundation of China (No. 12162024), the Jiangxi Province Outstanding Youth Talent Funding Program (No. 20192BCB23003), and the Jiangxi Natural Science Foundation (Nos. 20232BAB211017 and 20224BAB201019).

■ REFERENCES

(1) Barile, C.; Casavola, C.; De Cillis, F. Mechanical comparison of new composite materials for aerospace applications[J]. *Composites Part B: Engineering* **2019**, *162*, 122−128.

(2) Tiwary, A.; Kumar, R.; Chohan, J. S. A review on characteristics of composite and advanced materials used for aerospace applications-[J]. *Materials Today: Proceedings* **2022**, *51*, 865−870.

(3) Norkhairunnisa, M.; Hua, T. C.; Sapuan, S. M.et al.Evolution of aerospace composite materials *Advanced Composites in Aerospace Engineering Applications*. Springer International Publishing: Cham, 2022: 367−385.

(4) Skoczylas, J.; Samborski, S.; Kłonica, M. The application of composite materials in the aerospace industry. *J. Technol. Exploit. Mech. Eng.* **2019**, *5* (1), 1−6.

(5) Tian, X.; Zhou, K. 3D printing of cellular materials for advanced electrochemical energy storage and conversion[J]. *Nanoscale* **2020**, *12* (14), 7416−7432.

(6) Shahrubudin, N.; Lee, T. C.; Ramlan, R. An overview on 3D printing technology: Technological, materials, and applications[J]. *Procedia Manufacturing* **2019**, *35*, 1286−1296.

(7) Zastrow, M. The new 3D printing[J]. *Nature* **2020**, *578* (7793), 20−23.

(8) MacDonald, E.; Wicker, R. Multiprocess 3D printing for increasing component functionality. *Science* **2016**, *353* (6307), aaf2093.

(9) Ford, S.; Minshall, T. Invited review article: Where and how 3D printing is used in teaching and education[J]. *Additive Manufacturing* **2019**, *25*, 131−150.

(10) Dong, K.; Liu, L.; Huang, X.; et al. 3D printing of continuous fiber reinforced diamond cellular structural composites and tensile properties[J]. *Composite Structures* **2020**, *250*, No. 112610.

(11) Zhao, J.; Song, S.; Mu, X.; et al. Programming mechanoluminescent behaviors of 3D printed cellular structures[J]. *Nano energy* **2022**, *103*, No. 107825.

(12) Liu, Z.; Wang, S.; Shao, J.; et al. 3D radar stealth composite hierarchical grid structure with extremely broadband absorption performance and effective load bearing[J]. *Composites Part B: Engineering* **2022**, *247*, No. 110316.

(13) Song, S.; Xiong, C.; Yin, J.; et al. Mechanical property of all-composite diamond honeycomb sandwich structure based on interlocking technology: Experimental tests and numerical analysis. *Mech. Adv. Mater. Struct.* **2022**, 973−989.

(14) Hegde, S. R.; Hojjati, M. Thermally induced microcracks and mechanical property of composite honeycomb sandwich structure: experiment and finite element analysis[J]. *Journal of Sandwich Structures & Materials* **2020**, *22* (8), 2544−2566.

(15) Du, Z. H.; Ma, S. B.; Han, G. Q.; et al. The parameter optimization and mechanical property of the honeycomb structure for Ti_2AlNb based alloy[J]. *Journal of Manufacturing Processes* **2021**, *65*, 206−213.

(16) Xia, P.; Liu, Q.; Fu, H.; et al. Mechanical properties and energy absorption of 3D printed double-layered helix honeycomb under in-plane compression[J]. *Composite Structures* **2023**, *315*, No. 116982.

(17) Zhong, R.; Ren, X.; Zhang, X. Y.; et al. Mechanical properties of concrete composites with auxetic single and layered honeycomb structures[J]. *Construction and Building Materials* **2022**, *322*, No. 126453.

(18) Dong, Z.; Li, Y.; Zhao, T.; et al. Experimental and numerical studies on the compressive mechanical properties of the metallic auxetic reentrant honeycomb[J]. *Materials & Design* **2019**, *182*, No. 108036.

(19) Xu, H. H.; Luo, H. C.; Zhang, X. G.; et al. Mechanical properties of aluminum foam filled re-entrant honeycomb with uniform and gradient designs[J]. *International Journal of Mechanical Sciences* **2023**, *244*, No. 108075.

(20) Zhang, S.; Chen, W.; Gao, D.; et al. Experimental study on dynamic compression mechanical properties of aluminum honeycomb structures[J]. *Applied Sciences* **2020**, *10* (3), 1188.

(21) Lvov, V. A.; Senatov, F. S.; Korsunsky, A. M.; et al. Design and mechanical properties of 3D-printed auxetic honeycomb structure[J]. *Materials Today Communications* **2020**, *24*, No. 101173.

(22) Luo, H. C.; Ren, X.; Zhang, Y.; et al. Mechanical properties of foam-filled hexagonal and re-entrant honeycombs under uniaxial compression[J]. *Composite Structures* **2022**, *280*, No. 114922.

(23) Hou, W.; Shen, Y.; Jiang, K.; et al. Study on mechanical properties of carbon fiber honeycomb curved sandwich structure and its application in engine hood[J]. *Composite Structures* **2022**, *286*, No. 115302.

(24) Zhang, L.; Liu, B.; Gu, Y.; et al. Modelling and characterization of mechanical properties of optimized honeycomb structure[J].

International Journal of Mechanics and Materials in Design **2020**, *16*, 155−166.
(25) Zhan, B.; Hao, Y.; Qi, X.; et al. Multifunctional cellular carbon foams derived from chitosan toward self-cleaning, thermal insulation, and highly efficient microwave absorption properties. *Nano Res.* **2023**, *17*, 927−938.
(26) Jiang, P.; Zheng, H.; Xiong, J.; et al. A stabilized local RBF collocation method for incompressible Navier−Stokes equations[J]. *Computers & Fluids* **2023**, *265*, No. 105988.
(27) Xu, Z.; Li, J.; Li, J.; et al. Bionic structures for optimizing the design of stealth materials[J]. *Phys. Chem. Chem. Phys.* **2023**, *25* (8), 5913−5925.
(28) Indrusiak, T.; Soares, B. G.; Pereira, I. M.; et al. Low cost and easily scalable microwave absorbing material based on three-layer honeycomb sandwich structures[J]. *Materials Today Communications* **2023**, *35*, No. 105955.
(29) Xiao, J.; Qi, X.; Wang, L.; et al. Anion regulating endows core@ shell structured hollow carbon spheres@MoSxSe2−x with tunable and boosted microwave absorption performance. *Nano Res.* **2023**, *16*, 5756−5766.
(30) Jia, T.; Hao, Y.; Qi, X.; et al. Interface engineering and impedance matching strategy to develop core@ shell urchin-like NiO/Ni@ carbon nanotubes nanocomposites for microwave absorption[J]. *Journal of Materials Science & Technology* **2024**, *176*, 1−12.
(31) Xiang, L.; Darboe, A. K.; Luo, Z.; et al. Constructing two-dimensional/two-dimensional reduced graphene oxide/MoX2 (X = Se and S) van der Waals heterojunctions: a combined composition modulation and interface engineering strategy for microwave absorption. *Adv. Compos. Hybrid Mater.* **2023**, *6* (6), 215.
(32) Song, S.; Xiong, C.; Tao, F.; et al. Size effect of composite Kagome honeycomb sandwich structure reinforced with PMI foams under quasi-static bending: Experiment tests and numerical analysis-[J]. *Composite Structures* **2022**, *296*, No. 115832.
(33) Jin, T.; Zhou, Z.; Wang, Z.; et al. Experimental study on the effects of specimen in-plane size on the mechanical behavior of aluminum hexagonal honeycombs[J]. *Materials Science and Engineering: A* **2015**, *635*, 23−35.
(34) Pham, R. D.; Hütter, G. Influence of topology and porosity on size effects in stripes of cellular material with honeycomb structure under shear, tension and bending[J]. *Mech. Mater.* **2021**, *154*, No. 103727.
(35) Qi, C.; Jiang, F.; Yang, S. Advanced honeycomb designs for improving mechanical properties: A review[J]. *Composites Part B: Engineering* **2021**, *227*, No. 109393.
(36) Selim, M. M.; El-Safty, S.; Tounsi, A.; et al. Review of the impact of the external magnetic field on the characteristics of magnetic nanofluids[J]. *Alexandria Engineering Journal* **2023**, *76*, 75−89.
(37) Mohapatra, M.; Anand, S. Synthesis and applications of nano-structured iron oxides/hydroxides−a review. *Int. J. Eng., Sci. Technol.* **2010**, *2* (8), 127 DOI: 10.4314/ijest.v2i8.63846ISSN.
(38) Zunjarrao, S. C.; Singh, R. P. Characterization of the fracture behavior of epoxy reinforced with nanometer and micrometer sized aluminum particles[J]. *Compos. Sci. Technol.* **2006**, *66* (13), 2296−2305.
(39) Domun, N.; Hadavinia, H.; Zhang, T.; et al. Improving the fracture toughness and the strength of epoxy using nanomaterials−a review of the current status[J]. *Nanoscale* **2015**, *7* (23), 10294−10329.
(40) Zhu, D.-M.; Ding, F.; Haiping, Liu; et al. Mechanical properties of a photosensitive resin. *Chin. J. Eng. Sci.* **2019**, *41* (4), 512−520.
(41) Li, C.; Song, X. Surface Size-and Structure-Optimized Design of Two-Dimensional MXene Nanosheets for Electromagnetic Wave Absorption[J]. *ACS Applied Nano Materials* **2023**, *6* (13), 12050−12062.
(42) Hua, Z.; Chenghuan, L.; ChangAn, N.; et al. Study on Wave Absorption and Multilayer Optimum Design of γ-Fe 2 O 3 /Graphene Oxide/Ultrahigh-Performance Concrete Sheet. *Adv. Eng. Mater.* **2023**, *25* (6), 2201224.
(43) Hui, Z.; Yaohui, G.; Xinhua, S.; et al. Study on large-scale spatial absorption and attenuation characteristics of γ-Fe_2O_3 particles in different modes[J]. *Materials Today Communications* **2023**, *34*, No. 105297.
(44) GBT 1447−2005, *Test method for tensile properties of fiber-reinforced plastics* [S].
(45) *GBT 1448−2005 Test method for compression properties of fiber-reinforced plastics* [S].

https://doi.org/10.1021/acsomega.3c10138
ACS Omega 2024, 9, 14287−14296